Numerical Simulation of the FNG Wing Section in Turbulent Inflow

Jens Müller, Maximilian Ehrle, Thorsten Lutz, and Ewald Krämer

Abstract The influence of atmospheric turbulence on an extruded airfoil of the FNG wing in clean configuration is investigated using numerical simulation. Turbulence is injected into the flow field using a momentum source term. It is shown that the turbulence can be propagated accurately to the airfoil. Spectra of the pressure coefficient at different chordwise positions indicate a correlation between the inflow velocity spectrum and the local c_p spectra, especially for low to medium wave numbers. Furthermore, the applicability of the simplified Disturbance Velocity Approach (DVA) is evaluated, where the velocities of the atmospheric turbulence are added to the flux balance using superposition. The DVA shows satisfying results for the lift spectrum and the c_p spectrum at the leading edge over a broad wave number range. An overestimation of the amplitudes for the pitching moment and c_p spectra at $x/c = 0.2$ occurs at medium to high wave numbers. A scaling test of the TAU code in a development version with the implemented DVA is performed on this test case and shows satisfying scalability.

1 Introduction

Especially when flying at low altitudes, aircraft interact with atmospheric turbulence involving a broad wave number range. This interaction affects aerodynamic performance, passenger comfort, and leads to dynamic loads on the aircraft structure. According to the "Certification Specifications for Large Aeroplanes" CS-25 [2] gust as well as turbulence loads have to be taken into account in the aircraft design process. Hence, in the early phases of design it is necessary to understand and evaluate the effects of atmospheric turbulence on aircraft. Experimental investigations with grid generated turbulence were carried out, among others, by Hoffmann [6] and Hancock and Bradshaw [3]. These investigations show that free stream turbulence increases the maximum lift coefficient and also affects the level of turbulence kinetic

J. Müller (✉) · M. Ehrle · T. Lutz · E. Krämer
Institute of Aerodynamics and Gas Dynamics (IAG), University of Stuttgart, Pfaffenwaldring 21, 70569 Stuttgart, Germany
e-mail: jens.mueller@iag.uni-stuttgart.de

W. E. Nagel et al. (eds.), *High Performance Computing in Science and Engineering '19*,
https://doi.org/10.1007/978-3-030-66792-4_29

energy in the boundary layer. Numerical simulations of statically and dynamically disturbed inflow were carried out, for example, by Wawrzinek et al. [15]. Resolving atmospheric disturbances in numerical simulations requires high resolution of the computational grid and therefore high computational resources. However, an industrial application, for instance, in the aircraft certification process, requires a fast, cost-effective calculation. Therefore, Heinrich and Reimer [4] implemented a simplified method for simulating atmospheric disturbances, the so-called Disturbance Velocity Approach (DVA), into the flow solver TAU. Atmospheric disturbances are not propagated inside the flow field but added to the flux balance by superposition. This method has been successfully used for interactions of wake vortices and $1 - \cos$ gusts for gust wavelengths larger than twice the chord length c, see [4] and [5]. In the present test case the unsteady aerodynamic response of an extruded airfoil encountering broadband atmospheric turbulence is investigated. A reference case where the turbulence is resolved in the flow field is analyzed and compared to the simplified DVA.

2 Numerical Methods

Two different methods for representing atmospheric disturbances in CFD simulations are used within this work. As a reference case the atmospheric turbulence is fed into the flow field and then resolved within the discretized flow field. Consistent with Heinrich and Reimer [5] this physically correct method is called the Resolved Atmosphere Approach (RAA). The RAA simulations are carried out using the block structured FLOWer code developed by the German Aerospace Center (DLR) [9]. In recent years the spatial accuracy of FLOWer was enhanced by IAG from second to fifth order by implementation of a WENO scheme [13]. The high spatial accuracy allows for an accurate propagation and conservation of resolved atmospheric turbulence inside the CFD simulation necessary for the RAA. The DVA simulation is carried out using the unstructured flow solver TAU [12] since this approach is currently not available in FLOWer.

2.1 Resolved Atmosphere Approach

Simulating gust interaction, Heinrich and Reimer [4] use an unsteady far field boundary to feed the gust velocities into the flow field. A moving Chimera gust transport grid is applied in order to avoid numerical losses during gust propagation. While this approach is suitable for limited discrete signals, it is not applicable to broadband atmospheric turbulence. For statistical evaluations of the wing section's response to atmospheric turbulence, a large turbulence field is required. Hence, the Chimera transport grid cannot be applied and the turbulence has to be propagated from the far field domain to the airfoil. Since this distance is usually between $50c$ and $100c$, sig-

nificant numerical losses occur during the propagation. With the spatial second order of TAU this approach is not applicable to simulations with broadband atmospheric turbulence.

To solve this issue the turbulence is fed into the flow field using a momentum source term instead of prescribing unsteady velocities at the far field. An essential advantage of this method is that the turbulence can be fed in at any position within the CFD grid. Hence, the turbulence injection plane can be shifted close to the airfoil, significantly reducing the amount of grid cells as well as numerical losses. This method has been implemented in the FLOWer code and successfully used in wind energy simulations, such as wind turbines with atmospheric turbulence on a complex terrain [11]. The velocities of the atmospheric turbulence field $\mathbf{u}'$ are transformed into a volume force $\mathbf{f}_s$, which is needed to accelerate the mean velocity field $\bar{\mathbf{u}}$ to $\bar{\mathbf{u}} + \mathbf{u}'$. The source term is applied to a plane perpendicular to the inflow. In FLOWer the source term formulation

$$\mathbf{f}_s = \frac{\rho \mathbf{u}'}{\Delta x} \left(\bar{u}_n + \frac{1}{2} u'_n \right) \tag{1}$$

of Troldborg [14] is applied where the velocities with the index n and the grid spacing Δx are perpendicular to the turbulent inflow plane. Since the atmospheric turbulence is fed in and propagated in the flow field, both the interactions of turbulent fluctuations with the airfoil as well as the interactions of the flow around the airfoil with the turbulent inflow are considered.

2.2 Disturbance Velocity Approach

The DVA is a simplified approach for the representation of atmospheric disturbances in CFD simulations. Unlike the RAA the atmospheric turbulence is not propagated in the flow domain. The disturbance velocities from the atmospheric turbulence $\mathbf{u}'$ are added to the flux balance of each cell while the convection across the cell interfaces changes from $\mathbf{u} - \mathbf{u}_b$ to $\mathbf{u} - \mathbf{u}_b - \mathbf{u}'$, which deactivates the convection of the disturbance velocities in the flow field. According to Heinrich and Reimer [4] the continuity equation can be written as

$$\frac{d}{dt} \int_V \rho \, dV + \oint_S \rho (\mathbf{u} - \mathbf{u}_b - \mathbf{u}') \cdot \mathbf{n} \, dS = 0 \, . \tag{2}$$

For a detailed description of the DVA, see [4] and [5]. Since the turbulent fluctuations are not convected across the cell interfaces, no refinement of the grid compared to standard CFD simulations is needed, which leads to a significant reduction in computational costs. The main drawback is that the influence of the flow around the aircraft on the turbulence field is not considered since the turbulent fluctuations

remain unchanged during the simulation. In gust simulations this leads to inaccuracies in the DVA results for length scales smaller than twice the chord length [4], which is also expected for simulations with atmospheric turbulence.

2.3 *Inflow Turbulence Generation*

The atmospheric turbulence is created prior to the numerical simulations based on the model proposed by Mann [8]. The second order statistics of the velocity tensor are modeled using Taylor's frozen turbulence hypothesis. The model is based on the von Kármán isotropic spectrum in combination with the rapid distortion theory. Using an inverse Fourier transform the modeled atmospheric turbulence spectrum is transformed into a three dimensional velocity field. This velocity field is then passed to the flow solvers FLOWer and TAU and fed into the simulation using RAA and DVA respectively.

3 Setup

The wing of the "Flugzeug nächster Generation" (FNG, in English "next generation aircraft") [1] in clean configuration is used as a reference configuration within this work as a representative for today's conventional transport aircraft. The aspect ratio of the wing is $\lambda = 9.1441$ with a mean aerodynamic chord of $l_\mu = 5.15m$. The reference inflow condition for the current investigation is subsonic flow at $M = 0.25$ and $Re = 11.6 \times 10^6$ with respect to the mean aerodynamic chord of the FNG wing. The angle of attack is $\alpha = 4°$. In order to reduce the aerodynamic complexity an airfoil section at $\eta = 0.7$ is chosen for the current investigations. The airfoil section in the line of flight is transformed based on the local quarter-chord sweep angle. The inflow data and angle of attack are transformed accordingly. In the spanwise direction the airfoil section is extruded by $4l_\mu$. The extruded section of the FNG wing has a chord length of $c = 2.7m$ and is shown in Fig. 1. Isotropic atmospheric inflow turbulence based on the von Kármán spectrum is generated using the Mann model described in Sect. 2.3. A length scale $L = 5.15m$ with 5% turbulence intensity relative to the inflow velocity is chosen, where L is the length scale of the von Kármán energy spectrum [8]. The length scale is selected to lie within the valid range of the DVA for gust interactions with the smaller scales of the turbulent spectrum covering the critical range of the DVA to be accurate. This enables a reliable statement with regard to the applicability of the DVA for simulations with broadband atmospheric turbulence. The atmospheric turbulence field completely covers the extruded airfoil in the spanwise direction and is extended $\pm 3L$ above and below the airfoil. In the RAA simulation the turbulence is fed in at a distance of $5L$ upstream from the leading edge. This distance corresponds to the starting point of the turbulence for the DVA simulation.

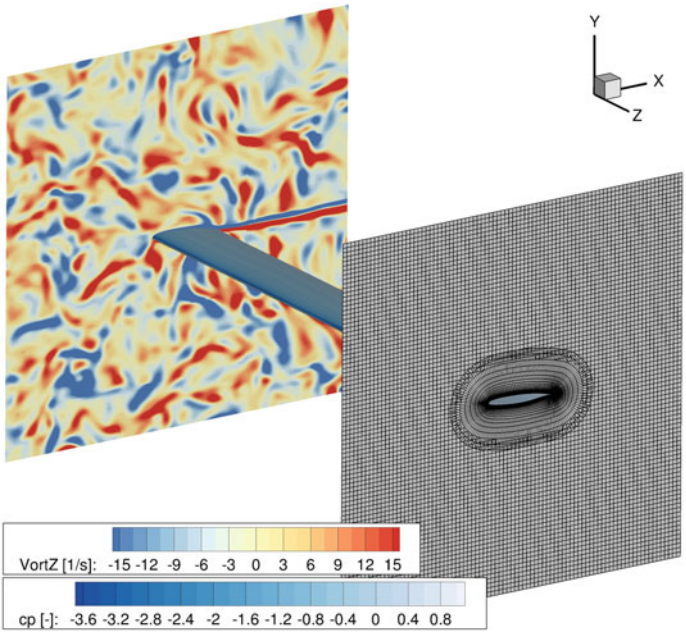

Fig. 1 Simulation setup: Extruded airfoil section with the corresponding grid used for RAA and DVA simulations. Every second grid point is shown in the figure. The contour plot shows the c_p distribution of the airfoil and the z-vorticity of the RAA in the flow field

A structured O-mesh was created around the airfoil with 144 cells along the upper and lower sides of the airfoil and 32 cells along the blunt trailing edge. The spanwise direction is resolved by 256 cells of constant grid spacing $\frac{L}{\Delta z} = 64$. $y^+ \leq 1$ is ensured in the first cell of the boundary layer. The mesh of the airfoil section is identical for FLOWer and TAU and integrated into a cartesian background mesh using the Chimera technique. The Chimera technique is also applied for the representation of the angle of attack as shown in Fig. 1. For the RAA simulations in FLOWer a fine grid resolution is needed in the turbulence propagation region to avoid significant numerical losses. Hence, a cartesian grid with $\frac{L}{\Delta x} = \frac{L}{\Delta y} = \frac{L}{\Delta z} = 64$ was created ranging from $5.25L$ upstream from the airfoil's leading edge to $5.75L$ downstream from the leading edge. In the y-direction the fine grid covers the complete field of turbulence. Further away from the airfoil the grid is coarsened using hanging grid nodes in order to save computational resources. To avoid any grid based numerical differences, the TAU background grid is equivalent to the FLOWer background grid in the vicinity of the airfoil section. Since the DVA does not require a highly resolved mesh in the propagation region, the high-resolution cartesian grid only covers the region between $2L$ upstream and $3L$ downstream from the leading edge in the TAU simulation. The grid is then slightly coarsened using unstructured tetrahedra to save mesh points. The far field distance for both FLOWer and TAU is $100c$. This results

in about 150 million cells for the RAA and about 113 million cells for the DVA simulation. In FLOWer, periodic boundary conditions are applied in the spanwise direction. In the TAU release 2014.2.0 used within this work, the combination of periodic boundary conditions and the Chimera overset grid is not possible. Since the symmetry plane boundary condition led to singularities at the connection of the wing section and symmetry plane with the DVA, the Euler wall boundary conditions is applied in TAU in the spanwise direction. The error is expected to be negligible when evaluating the results at a sufficient distance from the spanwise boundaries. For both approaches unsteady RANS simulations are performed and the Spalart-Allmaras turbulence model is applied since the angle of attack is chosen to be out of the range in which separation occurs. A fully turbulent boundary layer is assumed. Apart from the deviations that cannot be eliminated like the different grid metrics, the numerical parameters of FLOWer and TAU are chosen to be consistent. The physical time step size of $2.37 \cdot 10^{-4} s$ corresponds to a local CFL number $CFL_l = \frac{u_\infty \Delta t}{\Delta x} \approx 0.22$, ensuring an accurate propagation of the turbulent fluctuations. The convective time cycle of the wing section corresponds to 150 time steps.

4 Results

Prior to the simulations of the FNG airfoil section in atmospheric turbulence the accurate propagation of the resolved turbulence from the turbulent inflow plane to the airfoil's position has to be analyzed for the RAA. The results of this preliminary investigation are presented in Sect. 4.1. The effect of the inflow turbulence on the pressure spectra at the airfoil surface is analyzed in Sect. 4.2. Finally, the results of the RAA and DVA are compared with regard to the applicability of the DVA.

4.1 Propagation of Inflow Turbulence Using the RAA

The accurate propagation of atmospheric turbulence in FLOWer using the Mann model in combination with a WENO scheme and the momentum source term described in Sect. 2.1 has been proven by Kim et al. [7] and Schulz [10] for low Mach number flows typical for wind turbine simulations. The inflow Mach number considered in this work is significantly higher than it is in the work of Kim et al. or Schulz. Therefore, the propagation of the inflow turbulence for the present test case is analyzed for the highly resolved region of the cartesian mesh presented in Sect. 3 with a grid resolution of $\frac{L}{\Delta x} = \frac{L}{\Delta y} = \frac{L}{\Delta z} = 64$ without the airfoil present. The statistics of the propagated turbulence are evaluated at a distance $5L$ downstream from the turbulent inflow plane, where the leading edge is located in the main simulation with the airfoil. Figure 2 shows the power spectral density (PSD) of u, v, and w velocities at a distance $5L$ downstream from the inflow plane compared to the u velocity PSD of the Mann box, which is the turbulent data fed into the simulation. The v and w

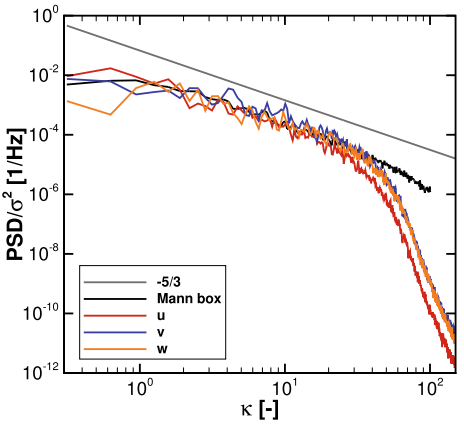

Fig. 2 PSD of u, v, and w velocities at a distance $5L$ downstream from the turbulent inflow plane compared to the u velocity PSD of the Mann box and the Kolmogorov $-5/3$ slope

Table 1 Degree of isotropy, turbulence kinetic energy, and turbulence intensity for the turbulent input data (Mann box) and FLOWer (RAA) without the airfoil at a distance 5L downstream from the turbulent inflow plane

	σ_u/σ_v	σ_u/σ_w	$k[m^2/s^2]$	$TI[\%]$
Mann box	1.004	1.001	21.357	5.00
FLOWer, RAA $5L$ downstream	0.993	1.015	17.387	4.51

velocity spectra for the Mann box are not shown here since the difference to the u velocity spectrum is negligible for isotropic turbulence. The Kolmogorov $-5/3$ slope is given as a reference for the inertial sub-range. The wave number κ is normalized with the turbulent length scale L according to Kim et al. [7] with $\kappa = \frac{2\pi f L}{u_\infty}$.

Figure 2 shows that the energy spectrum of the Mann box fed into the FLOWer simulation is conserved during the propagation for a broad wave number range for all three velocity components. The Mann box and the propagated velocity spectra follow the Kolmogorov $-5/3$ slope. Hence, the inertial sub-range is captured in the inflow data as well as in the propagated turbulence. At higher wave numbers the propagated spectra drop since the chosen grid resolution is no longer able to conserve and resolve these small scales. The drop occurs at $\kappa = 32$ for v and w and at $\kappa = 28$ for the u velocity. In addition to the energy spectra, the propagated turbulence also conserves the isotropy of the flow as shown in Table 1. Consistent with Kim's observations for low Mach number flows [7], the turbulence kinetic energy (TKE) k decays with increasing propagation distances. Thus, the target turbulence intensity (TI) of 5% specified in Sect. 3, which corresponds to the TKE $k = 21.357 \frac{m^2}{s^2}$ of the Mann box, is not reached at the airfoil's leading edge. This effect is compensated for the RAA simulation with the airfoil section by scaling the input data for the RAA simulation with a scaling factor $SF = \sqrt{k_0/k} = 1.1$ as proposed by Kim et al. [7]. k_0 is the TKE of the Mann box and k the TKE of the propagated turbulence at a distance

$5L$ downstream from the turbulent inflow plane, where the airfoil is located in the subsequent simulations. With the scaling for the RAA it is ensured that the wing section interacts with turbulence of the same turbulence intensity for both the RAA and DVA simulations.

It can be concluded that the statistics of the atmospheric turbulence can be propagated correctly to the airfoil. The isotropy as well as the energy spectra are conserved and the loss in turbulence kinetic energy is offset by scaling the input data for the RAA simulation. This allows an accurate analysis of the wing section in turbulent inflow with the RAA and a reliable comparison to the DVA simulation.

4.2 Wing Section in Turbulent Inflow

Having ensured the accurate propagation of the turbulence to the airfoil for the RAA simulation, the wing section is included in the simulation. The evaluation of the results in the following sections start after about six turbulent length scales have passed over the airfoil. This ensures that the initial interaction of the wing section and turbulence is not taken into account for the statistical evaluations. The statistics are averaged over 10400 time steps for both the RAA and DVA simulations. All statistics are evaluated in the spanwise center of the wing section as the statistical results do not change in the spanwise direction. Additionally, it is ensured that the influence of the different boundary conditions can be neglected.

In the present simulations, the reference length scale of the inflow turbulence of $L = 5.15m$ is about twice as large as the chord length of the wing section. Accordingly, the main effect expected for the airfoil is a variation of the local angle of attack. However, since broadband turbulence is interacting with the airfoil, smaller scales can have a significant influence as well. The time averaged pressure coefficient with corresponding standard deviations is shown in Fig. 3. It is compared to a steady solution without turbulence to assess relevant chordwise positions for further investigations. The result of the DVA is shown because there is no damping of high frequencies of the inflow turbulence using this approach.

The mean c_p distribution does not differ significantly from the steady solution without inflow turbulence. There is a slight reduction of the suction peak on the upper side of the airfoil. The differences diminish downstream until there is no significant deviation at $x/c = 0.5$. On the lower side of the airfoil the differences between the mean DVA result and the steady solution are considerably smaller. Looking at the standard deviations of the DVA c_p distribution the main effect of the interaction with atmospheric turbulence occurs at the leading edge and the suction peak, respectively. On the lower side of the airfoil and downstream from $x/c \approx 0.3$ the standard deviations are small so that only small scales are likely to play a role here, which can affect local separation bubbles and the laminar turbulent transition. Since the chosen angle of attack is below values at which separation occurs and the wing section is assumed to be fully turbulent, this is not investigated further within

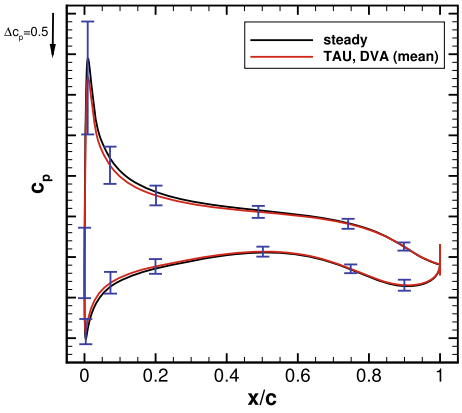

Fig. 3 Time averaged c_p distribution using DVA at $\eta = 0.5$ with corresponding standard deviations (blue) compared to a steady solution without atmospheric turbulence

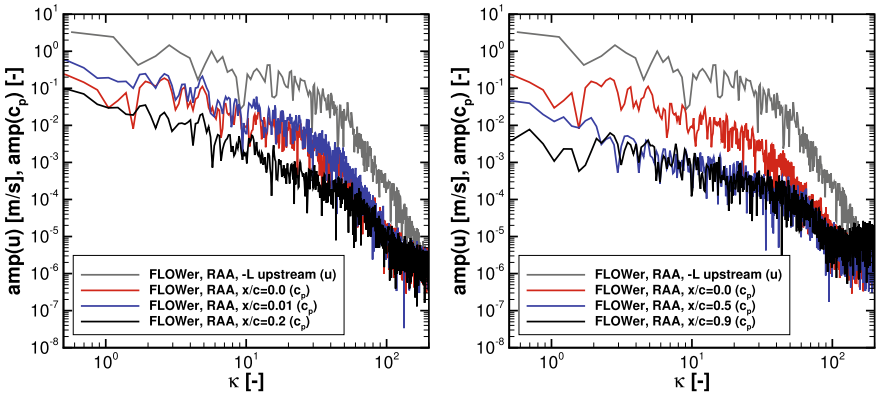

Fig. 4 FFT of the RAA c_p signal at different chordwise positions compared to the u velocity spectrum at a distance L upstream from the leading edge

this work. The impact on global loads at this part of the airfoil is expected to be small.

Based on the results presented in Fig. 3 the pressure coefficient of the RAA simulation at different chordwise positions is analyzed using a Fast Fourier Transform (FFT). Only the upper side of the airfoil is considered. The c_p spectra are compared to the u velocity spectrum at a distance L upstream from the leading edge. The RAA simulation represents the reference simulation for the later examination of the applicability of the DVA. On the left side of Fig. 4 the c_p spectra at $x/c = 0.0$, $x/c = 0.01$, and $x/c = 0.2$ are shown, where the first two positions correspond to the leading edge and the suction peak, respectively. The right side of Fig. 4 shows the c_p spectra at $x/c = 0.5$ and $x/c = 0.9$ compared to the spectrum at the leading edge and the inflow velocity spectrum.

In general, the slope of the spectra at the leading edge, suction peak, and 20% chord follow the slope of the u velocity spectrum upstream from the airfoil for wave numbers $\kappa \leq 12$. This indicates a correlation between the spectrum of the turbulent inflow and the local pressure at the region where the highest standard deviations from the mean pressure coefficient occur, which is the most relevant region for the evaluation of global loads acting on the configuration. For $\kappa > 12$ the gradient of the c_p amplitudes on the leading edge and suction peak is increased compared to the velocity amplitude, resulting in a higher reduction of the c_p amplitudes for these wave lengths. The smaller scales of the atmospheric turbulence are damped in this region due to the high velocity gradients of the flow around the leading edge. In the wave number range $12 \leq \kappa \leq 18$ the amplitude at $x/c = 0.2$ is reduced compared to the inflow velocity and the c_p at the leading edge and the suction peak. For higher wave numbers the slope again corresponds to that of the inflow up to $\kappa \approx 48$. This indicates a change of the medium to small scales corresponding with $12 \leq \kappa \leq 18$ at this position. There is almost no difference in the magnitude of the amplitudes at $x/c = 0.0$ and $x/c = 0.01$, whereas the magnitude of the amplitudes further downstream is reduced significantly. This corresponds with lower c_p fluctuations on the airfoil at the downstream positions. Looking at the c_p spectra at $x/c = 0.5$ and $x/c = 0.9$ on the right side of Fig. 4 the global amplitudes are further reduced, which results in lower c_p fluctuations in the pressure distribution. The amplitude reduction is more significant for the larger scales than for higher wave numbers. For wave numbers $\kappa > 32$ the differences in the c_p amplitudes are related to the boundary layer since the inflow turbulence is not resolved for higher wave numbers as shown in Sect. 4.1.

4.3 Applicability of the DVA

While the basic influence of broadband atmospheric inflow turbulence on the wing section was analyzed in Sect. 4.2 the question arises to what extent the simplified DVA can represent the physical processes. In contrast to the RAA, where the impact of the airfoil on the development of the incoming atmospheric turbulence is covered, the DVA only captures the influence of the atmospheric turbulence on the wing section. Based on the analysis of the c_p fluctuations with the RAA, only the chordwise positions with the most significant changes, $x/c = 0.0$ and $x/c = 0.2$ are analyzed within this section. The c_p spectra at both positions are shown in Fig. 5 for the RAA and the DVA. Since the atmospheric turbulence interpolated on the cells using the DVA is the velocity field from the Mann box, the u velocity spectrum of the Mann box is given as reference in addition to the u velocity spectrum at a distance L upstream from the leading edge for the RAA simulation. The maximum wave number $\kappa = 32$ where the velocity spectra of the atmospheric turbulence can be conserved in the RAA simulation is highlighted in the plots.

At $x/c = 0.0$ the DVA c_p spectrum corresponds to the c_p spectrum of the RAA simulation up to $\kappa \approx 32$. For higher wave numbers the amplitudes of the DVA spec-

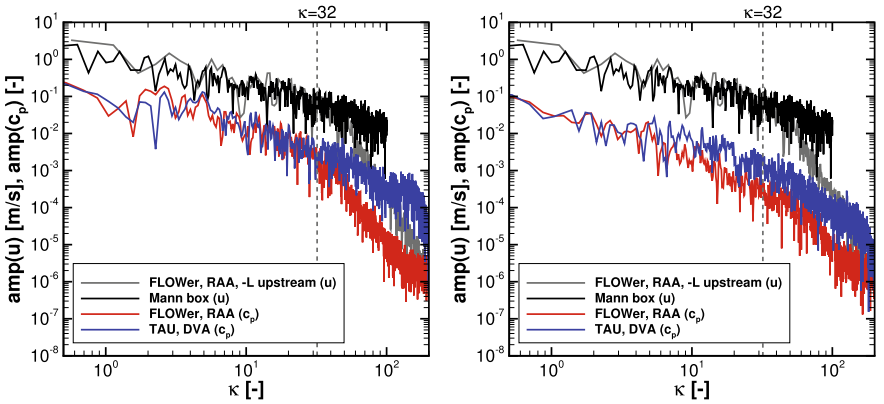

Fig. 5 FFT of the RAA and DVA c_p signal at different chordwise positions compared to the u velocity spectrum at a distance L upstream from the leading edge (RAA) and the one of the Mann box (DVA). left: $x/c = 0.0$, right: $x/c = 0.2$

trum are overestimated compared to the RAA. Since the velocity spectra of the atmospheric turbulence using the RAA can only be resolved up to $\kappa \approx 32$, as shown in Fig. 2, this is not a physical error of the DVA. For comparison at higher wave numbers the grid resolution in the RAA simulation has to be increased. The good agreement between RAA and DVA indicates that the feedback of the wing section's aerodynamics on the inflow turbulence is of minor importance at the leading edge. Hence, no significant change of atmospheric turbulence structures occurs at $x/c = 0$. Comparing the c_p spectrum of the DVA with the u velocity spectrum of the Mann box, it should be noted that the shapes correspond over the complete wave number range of the Mann box signal.

Further downstream the agreement between DVA and RAA decreases, as shown in the right part of Fig. 5. The c_p spectra at low wave numbers, i.e., the influence of the large scales, are well predicted by the DVA. However, for wave numbers $\kappa > 7$ the c_p amplitude is overestimated by the DVA. This indicates significant changes in the smaller scales of the inflow turbulence not covered by the DVA. The boundary layer thickness increases with increasing distance from the leading edge. Within the RAA simulation, the atmospheric turbulence interacts with the flow around the airfoil. This interaction influences the smaller scales of the inflow turbulence resulting in an amplitude reduction in the FFT. Since the inflow turbulence remains unchanged within the DVA, the effect of these scales on the pressure distribution is overestimated in comparison to the RAA.

The question arises how the overestimation of the c_p amplitudes with increasing x/c affects the global loads acting on the wing section. Therefore, the FFT of the lift and pitching moment history is plotted in Fig. 6. Taking the spectra of the lift signal, the DVA and RAA simulation match up to $\kappa \approx 25$. For higher wave numbers the amplitude of the lift spectrum is overestimated by the DVA compared to the RAA. As shown in Fig. 3 the major changes in the pressure coefficient, and thus also the

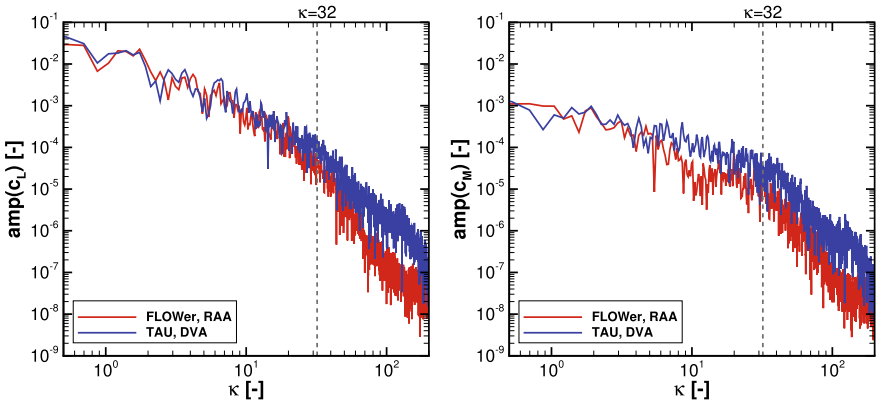

Fig. 6 FFT of the global loads for RAA and DVA. left: lift spectrum, right: pitching moment spectrum

main influence on the lift, occur at the area around the leading edge and the suction peak. At these positions, the DVA is capable of reproducing the RAA c_p spectrum up to $\kappa \approx 32$. Hence, the main influence on the lift is covered by the DVA. The c_p distribution of the positions further downstream, where the DVA lacks of agreement with the RAA, are of minor importance for the lift.

A different situation occurs when looking at the pitching moment around the quarter chord. Here, the amplitudes of RAA and DVA differ starting from $\kappa \approx 5$. While the c_p spectra of the DVA match the spectra of the RAA up to $\kappa \approx 32$ at the leading edge, the maximum wave number where the DVA c_p spectra correspond to the ones of the RAA decreases with increasing x/c as shown in Fig. 5. Due to the distance to the quarter chord the rear part of the airfoil is of significant influence when evaluating the pitching moment. The overestimation of the c_p amplitudes even for small wave numbers at this part of the airfoil directly influences the spectrum of the pitching moment. The larger distance to the quarter chord compensates the lower magnitude of the c_p amplitude compared to the leading edge. Hence, an accurate estimation of the RAA pitching moment with the DVA is only possible for small wave numbers.

5 Scaling Test

Improvements in runtime are mandatory in terms of effective use of valuable computational resources and enable more research simulations. This requires thorough testing of the scaling capabilities of the TAU code version 2014.2.0 with DVA implementation. It aims at investigating shortcomings of the implementation of the DVA routines, which are currently under development, as well as the overall performance of the code. In order to collect statistically relevant data for this test case, about

Table 2 Scaling test cases and according parameters

Case	Nodes	Cores	Points/Domain
1	9	216	163,460
2	18	432	81,730
3	37	888	39,760
4	74	1,776	19,880
5	148	3,552	9,940
6	296	7,104	4,970

8,800 node hours are required. This estimation is based on the assumption of 13,550 time steps on 37 nodes of the Cray XC-40 "Hazelhen". An effective use of computational resources requires a CFD code which scales well in terms of increasing number of nodes and thus an appropriate number of nodes for the present test case has to be chosen. For the investigation of the scaling behavior, the computational grid is decomposed in varying numbers of partitions. The simulations are performed accordingly with different node numbers resulting in a strong scaling test. Because the scaling test was conducted during the *Optimization of Scaling and Node-level Performance on Hazel Hen (Cray XC40)*, further performance data of the TAU code for this specific test case could be gathered and will be analyzed. This analysis is performed with *performance tools lite* by Cray and comprises a code sampling approach which only leads to minor influence on runtime. This enables a more in-depth analysis of code specific behavior. Thus, the scaling capabilities of each code routine can be analyzed separately.

The scaling test in the present work is performed on the DVA test case, which includes a hybrid grid with approx. 35 million grid points. Production runs presented in Sect. 4 are performed on 37 compute nodes with 888 cores which leads to approximately 40,000 grid points per domain. In order to investigate this code's scaling behavior, the node count is reduced to 18 and 9 nodes as well as extended to 74, 148 and 296 nodes respectively. Table 2 shows the scaling test cases with node numbers, core numbers and grid points per domain.

Figure 7 shows the influence of node number on the overall runtime of the test case. An increase from 9 nodes until 74 nodes leads to a nearly linear decrease of runtime. In comparison to previous TAU scaling tests, e.g., Wawrzinek et al. [15], which showed an almost linear scaling for the whole investigated node number range, a further increase of nodes decreases the advantage in runtime in the 148 nodes case and finally leads to an increase in overall runtime in case of 296 nodes. The difference of these results could be due to different versions of the TAU code as well as due to the not yet optimized implementation of the DVA, which is currently under development. This issue will be further investigated by means of a scaling analysis of the most time consuming TAU routines.

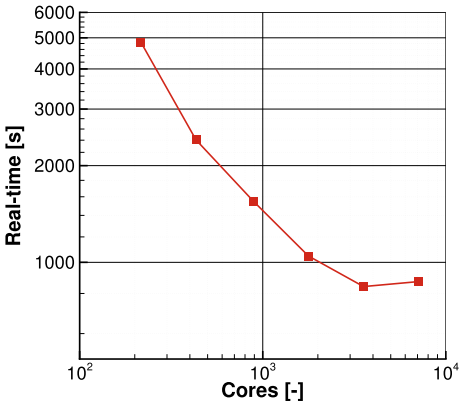

Fig. 7 Scaling of the present computational setup using TAU 2014.2.0 with implemented DVA. Scaling test cases according to Table 2. 15 physical time steps are used for the scaling test

5.1 Scaling of TAU Routines

Figure 8 shows the scaling behavior of the 9 most time-consuming routines of the TAU-Code by means of the percentage and absolute number of overall samples. The sampling approach of Cray's perftools lite samples the program counter at a time interval and delivers an absolute number of samples and the part of the overall runtime of each routine. The first two routines are attributed to MPI communication, routine 3 to 8 are functions implemented in the TAU solver, routine 9 is part of the DVA implementation and reads the turbulence data files. The first, most time consuming routine, shows a decrease in absolute samples and thus scales well in terms of an increasing number of nodes. The second routine does not scale well in terms of run time reduction when increasing the number of nodes. An increase of nodes leads to increasing percentage of samples on the overall computational time and an almost constant number of absolute samples between 18 and 296 nodes. The scaling behavior of these routines can be attributed to MPI communication, as an increase of nodes leads to an increase of data exchange between the different processes. Routines 3 to 8, which can be attributed to the TAU solver (e.g., calculation of fluxes and gradients) scale very well, which means less samples with increasing number of nodes for all test cases. The last routine shown in Fig. 8 is attributed to reading turbulence data for the DVA and therefore not part of the standard TAU implementation. It is clearly visible that the total number of samples stays constant with increasing node number, which is due to constant reading speed of the ASCII files containing turbulence data. This observation leads to a possible explanation of the overall scaling of this test case. While most of the standard routines of TAU show good scaling behavior, the part of reading gust data of the overall runtime increases with increasing number of nodes and therefore limits this code's scaling capabilities. As this part of the code is currently under development, the scaling analysis can be taken into account for optimization and parallel implementation of these routines e.g., by means of parallel reading of data.

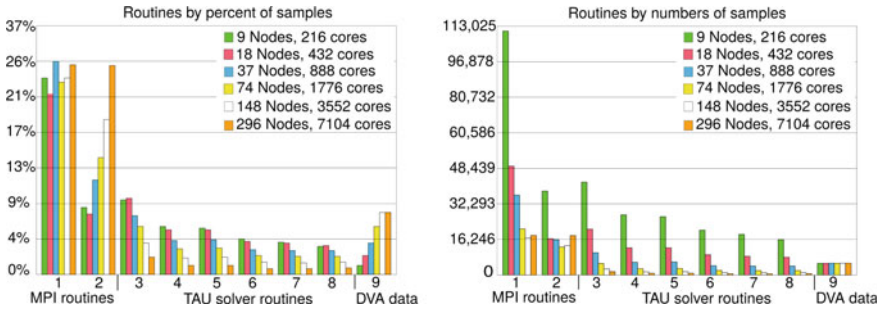

Fig. 8 Scaling behavior of the 9 most time consuming routines of this test case with the TAU solver, produced with Craypat pat view, relative and absolute number of samples

6 Conclusion

The influence of broadband atmospheric turbulence on an extruded airfoil was investigated in this study. The turbulence was fed in at a distance $5L$ upstream from the leading edge using a momentum source term. L represents the length scale of the atmospheric turbulence. It was shown that the turbulence can be propagated accurately from the turbulent inflow plane to the airfoil and isotropy is conserved within the flow. The main impact on the c_p distribution occurs at the leading edge and the suction peak. Up to a reduced wave number of $\kappa = 12$ the shape of the c_p spectra at this positions corresponds to that of the u velocity spectrum at a distance L upstream from the leading edge. Further downstream the amplitudes of the c_p spectra are reduced for small wave numbers with minor differences between $x/c = 0.5$ and $x/c = 0.9$. In addition to the effect of atmospheric turbulence on surface pressure and global loads, the applicability of the simplified DVA was investigated. At the leading edge the c_p spectrum of the DVA matches the one of the physically accurate RAA up to $\kappa = 32$, whereas the c_p spectrum of the DVA at $x/c = 0.2$ overestimates the c_p amplitudes for $\kappa > 7$. The lift spectrum of the DVA corresponds to the one of the RAA up to $\kappa = 25$, whereas the RAA pitching moment can only be estimated correctly by the DVA for $\kappa < 5$. Hence, the DVA is capable of covering the main effects of an airfoil in atmospheric turbulence in terms of lift spectrum and c_p spectra at leading edge and suction peak. It tends to overestimate the c_p spectra compared to the RAA at high wave numbers especially further downstream. Therefore, the RAA pitching moment can only be calculated correctly by the DVA for low wave numbers. Furthermore, the scaling capabilities of an extended version of the DLR TAU code that includes the DVA approach were investigated. This scaling test showed good scaling behavior of the TAU code with increasing node number, but revealed non-scaling routines of the DVA implementation. As this part of the code is currently under development, the results of this analysis could be taken into account for further implementation and optimization of the DVA routines.

Acknowledgements The authors gratefully acknowledge the Federal Ministry for Economic Affairs and Energy, which funded the work presented in this report as part of the LuFo project VitAM-Turbulence. Also, we acknowledge the High Performance Computing Center Stuttgart (HLRS) for the provision of computational resources and the continued support.

References

1. G. Dargel, H. Hansen, J. Wild, T. Streit, H. Rosemann, K. Richter, Aerodynamische Flügelauslegung mit multifunktionalen Steuerflächen. DGLR Jahrbuch p. 1605 (2002)
2. European Aviation Safety Agency, https://www.easa.europa.eu/sites/default/files/dfu/CS-25%20Amendment%2022.pdf: Certification Specifications and Acceptable Means of Compliance for Large Aeroplanes CS-25, Amendment 22. Accessed: 2019-04-27
3. P. Hancock, P. Bradshaw, Turbulence structure of a boundary layer beneath a turbulent free stream. J. Fluid Mech. **205**, 45–76 (1989)
4. R. Heinrich, L. Reimer, Comparison of Different Approaches for Gust Modeling in the CFD code Tau. International Forum on Aeroelasticity & Structural Dynamics (2013)
5. R. Heinrich, L. Reimer, Comparison of Different Approaches for Modeling of Atmospheric Effects like Gusts and Wake-Vortices in the CFD Code Tau. International Forum on Aeroelasticity & Structural Dynamics (2017)
6. J.A. Hoffmann, Effects of freestream turbulence on the performance characteristics of an airfoil. AIAA J. **29**(9), 1353–1354 (1991)
7. Y. Kim, P. Weihing, C. Schulz, T. Lutz, Do turbulence models deteriorate solutions using a non-oscillatory scheme? J. Wind Eng. Industr. Aerodynam. **156**, 41–49 (2016)
8. J. Mann, The spatial structure of neutral atmospheric surface-layer turbulence. J. Fluid Mech. **273**, 141–168 (1994)
9. J. Raddatz, J.K. Fassbender, Block structured Navier-Stokes solver flower, in *MEGAFLOW - Numerical Flow Simulation for Aircraft Design*, ed. by N. Kroll, J.K. Fassbender (Springer, Berlin Heidelberg, Berlin, Heidelberg, 2005), pp. 27–44
10. C. Schulz, Numerische Untersuchung des Verhaltens von Windenergieanlagen in komplexem Gelände unter turbulenter atmosphärischer Zuströmung. Ph.D. thesis, Institute of Aerodynamics and Gas Dynamics, University of Stuttgart (2017)
11. C. Schulz, L. Klein, P. Weihing, T. Lutz, Investigations into the interaction of a wind turbine with atmospheric turbulence in complex terrain. J. Phys. Conference Series **753**(3), 032016 (2016)
12. D. Schwamborn, T. Gerhold, R. Heinrich, The DLR TAU-Code, Recent Applications in Research and Industry. European Conference on Computational Fluid Dynamics ECCOMAS CFD (2006)
13. C. Stanger, B. Kutz, U. Kowarsch, E.R. Busch, M. Keßler, E. Krämer, Enhancement and Applications of a Structural URANS Solver. In: High Performance Computing in Science and Engineering '14, pp. 433–446. Springer (2015)
14. N. Troldborg, J.N. Sørensen, R. Mikkelsen, N.N. Sørensen, A simple atmospheric boundary layer model applied to large eddy simulations of wind turbine wakes. Wind Energy **17**(4), 657–669 (2014)
15. K. Wawrzinek, T. Lutz, E. Krämer, Numerical Simulations of Artificial Disturbance Influence on a High Lift Airfoil. In: High Performance Computing in Science and Engineering'17, pp. 323–337. Springer (2018)